

# Optical and Ultraviolet Monitoring of the Black Hole X-ray Binary MAXI J1820+070/ASASSN-18ey for 18 Months

Hanna Sai,<sup>1\*</sup> Xiaofeng Wang,<sup>1,2†</sup> Jianfeng Wu,<sup>3</sup> Jie Lin,<sup>1</sup> Hua Feng,<sup>4,5</sup> Tianmeng Zhang,<sup>6,7</sup> Wenxiong Li,<sup>1</sup> Jujia Zhang,<sup>8,9,10</sup> Jun Mo,<sup>1</sup> Tianrui Sun,<sup>11,12,13</sup> Shuhrat A. Ehgamberdiev,<sup>14</sup> Davron Mirzaqulov,<sup>14</sup> Liming Rui,<sup>1</sup> Weili Lin,<sup>1</sup> Xulin Zhao,<sup>15</sup> Han Lin,<sup>1</sup> Jicheng Zhang,<sup>1</sup> Xinghan Zhang,<sup>1</sup> Yong Zhao,<sup>6,16</sup> Xue Li,<sup>1</sup> Danfeng Xiang,<sup>1</sup> Lingzhi Wang,<sup>17,18</sup> Chengyuan W

<sup>1</sup>Physics Department and Tsinghua Center for Astrophysics (THCA), Tsinghua University, Beijing, 100084, China

<sup>2</sup>Beijing Planetarium, Beijing Academy of Science and Technology, Beijing, 100044, China

<sup>3</sup>Department of Astronomy Xiamen University (Haiyun Campus), Siming District, Xiamen, Fujian, 361005, China

<sup>4</sup>Department of Astronomy, Tsinghua University, Beijing, 100084, China.

<sup>5</sup>Department of Engineering Physics, Tsinghua University, Beijing, 100084, China.

<sup>6</sup>Key Laboratory of Optical Astronomy, National Astronomical Observatories, Chinese Academy of Sciences, Beijing, 100101, China

<sup>7</sup>School of Astronomy and Space Science, University of Chinese Academy of Sciences, 101408, Beijing

<sup>8</sup>Yunnan Observatories (YNAO), Chinese Academy of Sciences, Kunming 650216, China

<sup>9</sup>Key Laboratory for the Structure and Evolution of Celestial Objects, Chinese Academy of Sciences, Kunming 650216, China

<sup>10</sup>Center for Astronomical Mega-Science, Chinese Academy of Sciences, 20A Datun Road, Chaoyang District, Beijing, 100012, China

<sup>11</sup>Purple Mountain Observatory, Chinese Academy of Sciences, Nanjing 210008, China

<sup>12</sup>Chinese Center for Antarctic Astronomy, Nanjing 210008, China

<sup>13</sup>School of Astronomy and Space Science, University of Science and Technology of China, Hefei 230026, China

<sup>14</sup>Ulugh Beg Astronomical Institute, Uzbekistan Academy of Sciences, Tashkent, 100052, Uzbekistan

<sup>15</sup>School of Science, Tianjin University of Technology, Tianjin, 300384, China

<sup>16</sup>University of Chinese Academy of Sciences, Beijing 100049, China

<sup>17</sup>National Astronomical Observatory of China, Chinese Academy of Sciences, Beijing, 100012, China

<sup>18</sup>Chinese Academy of Sciences South America Center for Astronomy, National Astronomical Observatories, CAS, Beijing 100101, China

Accepted XXX. Received YYY; in original form ZZZ

## ABSTRACT

MAXI J1820+070 is a low-mass black hole X-ray binary system with high luminosity in both optical and X-ray bands during the outburst periods. We present extensive photometry in X-ray, ultraviolet, and optical bands, as well as densely-cadenced optical spectra, covering the phase from the beginning of optical outburst to  $\sim 550$  days. During the rebrightening process, the optical emission preceded the X-ray by  $20.80 \pm 2.85$  days. The spectra are characterized by blue continua and emission features of Balmer series, He I, He II lines and broad Bowen blend. The pseudo equivalent width (pEW) of emission lines are found to show anticorrelations with the X-ray flux measured at comparable phases, which is due to the increased suppression by the optical continuum. At around the X-ray peak, the full width at half maximums (FWHMs) of H $\beta$  and He II  $\lambda 4686$  tend to stabilize at 19.4 Angstrom and 21.8 Angstrom, which corresponds to the line forming region at a radius of 1.7 and 1.3  $R_{\odot}$  within the disk. We further analyzed the absolute fluxes of the lines and found that the fluxes of H $\beta$  and He II  $\lambda 4686$  show positive correlations with the X-ray flux, favoring that the irradiation model is responsible for the optical emission. However, the fact that X-ray emission experiences a dramatic flux drop at  $t \sim 200$  days after the outburst, while the optical flux only shows little variations suggests that additional energy such as viscous energy may contribute to the optical radiation in addition to the X-ray irradiation.

**Key words:** accretion, accretion discs - stars: black holes - X-rays: binaries

\* E-mail: shn17@mails.tsinghua.edu.cn

† E-mail: wang\_xf@mail.tsinghua.edu.cn

## 1 INTRODUCTION

Low-mass X-ray binaries (LMXBs) are close binary systems consisting of a compact object and a low-mass companion star having filled its Roche lobe. The mass-donor companion can be a main-sequence star, a subgiant, or a white dwarf (WD), while the compact object can be a black hole (BH) or a neutron star (NS). Materials of the donor star transfer to the compact object through the  $L1$  Lagrangian point, forming a surrounding accretion disc (Charles & Coe 2006; Gu et al. 2019). LMXBs often stay for years or decades in a state of quiescence with X-ray luminosities of  $\sim 10^{29} - 10^{33.5} \text{ erg s}^{-1}$  before turning into outbursts (Remillard & McClintock 2006). The mass of a BH in an X-ray binary can be determined based on the periodic variations inferred from the spectroscopic and photometric observations in quiescence (e.g., Casares & Jonker 2014; Wu et al. 2015, 2016). During the outburst, the luminosity of these LMXBs can increase by many orders of magnitudes relative to its quiescent state (Chen et al. 1997). The outbursts can be explained by instability of accretion discs surrounding the compact object (Osaki 1995; Lasota 2001; Dubus et al. 2001), which is also called the “thermal-viscous disc instability model” (DIM). Some LMXB transients can experience several outbursts, and those with higher mass transfer rate tend to have higher outburst frequencies (Lin et al. 2019).

According to the irradiated disk model, the optical and ultraviolet (UV) -band emissions are believed to arise from reprocessing of the X-ray emission (Rykoff et al. 2007; Gierliński et al. 2008, 2009). In this scenario, the temperature structure of the outer disc will be altered by the irradiated inner disk and Compton tail, leading to production of the observed optical/UV emission (Gierliński et al. 2009). The optical spectra of LMXBs often contain emission lines, such as the Balmer series. The emission lines are believed to originate from rotating accretion flow of the disc, which is ionized by irradiation from a central high-luminosity X-ray source. Note, however, that there are other arguments about the origin of the optical radiation of LMXB transients, such as the jet/corona (Eikenberry et al. 1998; Markoff et al. 2005; Russell et al. 2006) or the atmosphere of an optically thick disc in bright/soft X-ray states (Wu et al. 2001, 2002). Moreover, the  $H_{\alpha}$  emission line could also originate in a dense outflow in low/hard X-ray states (Wu et al. 2001). At low-luminosity state, the ionizing source is usually considered to be viscous heating of the disc (van Paradijs & McClintock 1994; Fender et al. 2009).

The outburst of the LMXB system, MAXI J1820+070 (ASASSN-18ey), was initially discovered as an optical transient ASASSN-18ey on UT Mar.06.58 2018 by the All Sky Automated Survey for SuperNovae (ASAS-SN; Shappee et al. 2014; Kochanek et al. 2017) at R.A. =  $18^{\text{h}}20^{\text{m}}21^{\text{s}}.9$ , dec. =  $+07^{\circ}11'07''.3$  (J2000)<sup>1</sup>. About one week later, the Monitor of All-sky X-ray Image (MAXI; Matsuoka et al. 2009) Gas Slit Camera (Mihara et al. 2011) nova alert system detected a bright X-ray transient at the same location with a flux of  $32 \pm 9 \text{ mCrab}$  in 4 - 10 keV (Kawamuro et al. 2018), which was designated as MAXI J1820+070. Multiwavelength follow-up observations suggested that MAXI J1820+070 is a BH LMXB (e.g., Baglio et al. 2018; Homan

et al. 2018; Tucker et al. 2018). The distance to this system is estimated as  $3.46^{+2.18}_{-1.03} \text{ kpc}$  according to the Gaia DR2 parallax data (Gandhi et al. 2019). Atri et al. (2020) provided a consistent and more precise measurement on the distance to MAXI J1820+070 as  $2.96 \pm 0.33 \text{ kpc}$  using the parallax obtained from radio interferometry.

The X-ray and optical monitoring of this system showed that there is a time lag of  $7.20 \pm 0.97$  days between the outbursts detected in optical and X-ray bands for MAXI J1820+070 in March, 2018 (Tucker et al. 2018). This delay suggests that the thermal instability initially triggered an outburst in the thermal-viscous disc. The X-ray and optical monitoring of this system suggests that the state transition is not only related to the mass accretion rate (Shidatsu et al. 2019). They proposed that the jet contributed to the optical emission in the low/hard state, whereas the outer disc emission dominated the optical flux in high/soft state. Polarization observations also favored for the existence of jet or hot flow for MAXI J1820+070 (Veledina et al. 2019). Dynamical modeling of MAXI J1820+070 system was carried out by Torres et al. (2019). They confirmed the property of stellar-mass BH for the compact primary of MAXI J1820+070, with its mass function as  $f(M) = 5.18 \pm 0.15 M_{\odot}$  and an orbital period of  $0.68549 \pm 0.00001$  days. Muñoz-Darias et al. (2019) detected P-Cygni profiles and broad wings in He I  $\lambda 5876$  and  $H_{\alpha}$  emission lines in the high-resolution optical spectra of MAXI J1820+070 taken during low/hard states, suggesting the existence of accretion disc wind.

In this paper, we report extensive follow-up observations of MAXI J1820+070 in optical, UV, and X-ray bands for about 18 months, and present its observational properties. The relations between optical/UV and X-ray features have been analyzed, with an attempt to better constrain the radiation physics for this BH binary system. The paper is organized as follows: in Section 2, the observations and data reductions are described. Section 3 presents the light/color curves, and Section 4 presents the spectral evolution. In Section 5, we discuss the properties of MAXI J1820+070, including spectral energy distribution (SED) and the correlation between optical and X-ray properties. We summarize our results in Section 6.

## 2 OBSERVATIONS AND DATA REDUCTION

After the discovery of MAXI J1820+070, we started a long-term spectroscopic and photometric monitoring campaign in optical bands. The follow-up photometric observations started on March 20, 2018, using the 0.8-m Tsinghua-NAOC Telescope (TNT) (Huang et al. 2012; see Figure 1 for a sample image) and the Yaoan High Precision Telescope in China, as well as the AZT-22 1.5-m telescope (hereafter AZT) at the Maidanak Astronomical Observatory in Uzbekistan (Ehgamberdiev 2018). We use standard IRAF routines to pre-process all CCD images, which include bias subtraction, flat fielding, and the removal of cosmic rays. Point-spread-function (PSF) photometry was performed for both the object and the reference stars using the pipeline *Zuruphot* developed for automatic photometry of TNT (Mo et al. in prep.). The instrumental magnitudes were then converted into those of the Johnsons *BV* (Johnson et al. 1966) and Sloan Digital Sky Survey (SDSS) *gri*-band system (Fukugita

<sup>1</sup> <http://www.astronomy.ohio-state.edu/asassn/transients.html>

et al. 1996). Table A1 lists the standard BV- and *gri*-band magnitudes of the comparison stars, which are also marked in Figure 1. MAXI J1820+070 was also observed by the Ultraviolet/Optical Telescope (UVOT; Roming et al. 2005) onboard the *Neil Gehrels Swift Observatory* (*Swift*; Gehrels et al. 2004) in three UV (*uvw2*, *uvm2* and *uvw1*) and three optical filters (*u*, *b* and *v*). The final calibrated magnitudes in the *Swift* filters are presented in Table A2 and Table A3, respectively. The *Swift* images of MAXI J1820+070 were reduced using the HEASOFT<sup>2</sup> with the latest *Swift* calibration database<sup>3</sup>.

We also analyzed the *Swift*/XRT observations of MAXI J1820+070 obtained during the period from MJD 58189 to MJD 58591. These observations were obtained in both window timing (WT) and photon count (PC) modes. All of the XRT data were first reduced by running the *xrtpipeline* task of HEASOFT (version 6.19). Since the count rate of MAXI J1820+070 can reach beyond 500 cps, the source region suffers serious pile-up effect. To avoid this effect, we extract the source photons using an annular region. The outer radius is set as 40 pixels, and the inner radius is adjustable according to the count rates. In the WT mode observations, the inner radius is set as RATE/100 pixels (RATE stands for the count rate). In the PC mode observations, the inner radius is fixed as 2 pixels if the count rate is higher than 0.5 cps; otherwise, the inner radius is set to zero. The background photons were estimated from an annular region with an outer radius of 120 pixels and an inner radius of 60 pixels. The energy spectra were extracted by the XSELECT package and grouped into bins with a minimum of 20 photons. We adopted response matrix files (RMFs) from the *Swift*/XRT calibration database (CALDB) and created ancillary response files (ARFs) from exposure maps using the *xrtmkarf* task. The XRT spectra between 0.6 and 10 keV were fitted with a model composed of a power-law component (the *powerlaw* model) plus a multi-black body component (the *diskbb* model). The power-law component accounts for the comptonized X-ray emission, and the multi-black body component represents the thermal X-ray emission from the surface of the accretion disc, while the X-ray absorption is characterized by the *wabs* model. During the phase from 336 to 371 days after the initial detection, the X-ray count rate is quite low so we use a single power-law model to estimate the flux (Kirsch et al. 2005).

A total of 66 spectra were obtained for MAXI J1820+070 with the Lijiang 2.4-m telescope (+YFOSC) and Xinglong 2.16-m telescope (+BFOSC and +OMR) (Zhang et al. 2016), covering the phases from +11.9 days to +385.3 days since the discovery. A log of the spectra is given in Table A4. We reduced all the spectra using standard IRAF routine. Flux calibration of the spectra was performed with spectrophotometric standard stars taken on the same nights. The spectra were corrected for atmospheric extinction using the extinction curves of local observatories; and the telluric lines were removed from the spectra.

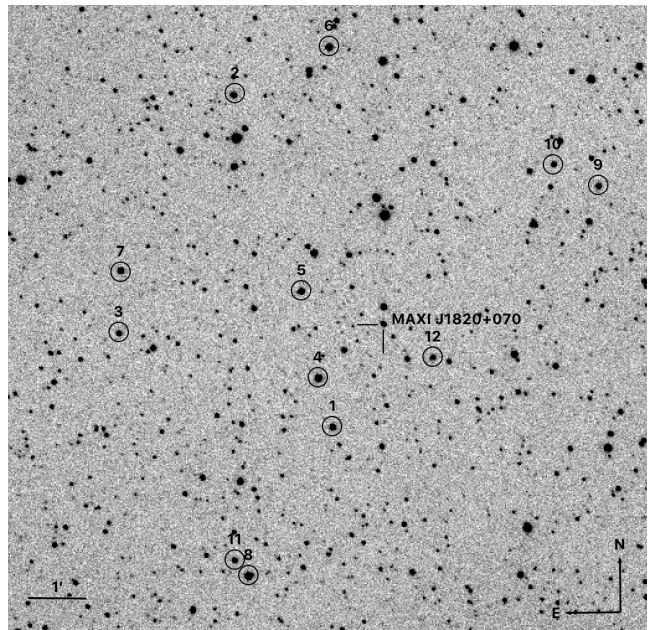


**Figure 1.** Image of MAXI J1820+070/ASASSN-18ey, taken with the Tsinghua-NAOC 0.8-m Telescope (TNT). North is up and east is to the left. MAXI J1820+070 is indicated by the solid thick sticks. The reference stars are labeled with black circles.

### 3 LIGHT CURVES

Figure 2 shows the optical and UV light curves of MAXI J1820+070, covering the phase from +6.92 to +536.67 days relative to the first detection of optical outburst. For the TNT observations, the first gap appeared between July and August, 2018, covering the phase from +114 to +185 days, is due to the maintenance of the telescope in the summer season, while the second gap, seen during the phase from  $t \sim +258$  to +372 days, is because that the source moved close to the sun. To complement the sampling of the light curves, we also collected the *B*-band data from the American Association of Variable Star Observers (AAVSO).

At  $t \sim +100$  days and 210 days after outburst, MAXI J1820+070 is found to exhibit two rebrightening behaviors. However, it did not show quiescence between these two epochs. The first rebrightening occurred before the transition from low/hard to high/soft states, while the second one occurred shortly after the transition from the high/soft to low/hard states. By  $t \sim +360$  days, this system faded gradually towards its quiescent state (Russell et al. 2019b). At  $t \sim +370$  days, however, this system is found to experience a post-outburst “rebrightening” in both optical and X-ray bands (Ulowetz et al. 2019; Bahramian et al. 2019), and reached a *B*-band peak of 14.17 mag at  $t \sim +380$  days. This corresponds to an absolute magnitude of 1.47 mag in *B* band using the Gaia distance (Gandhi et al. 2019). After that, MAXI J1820+070 tended to decrease in both X-ray and optical bands and entered into the quiescent state based on the X-ray flux reported by *Swift* and *NuSTAR* (Vozza et al. 2019; Tomsick & Homan 2019). At  $t \sim +507$  days, MAXI J1820+070 was found to rebrighten again in optical (see Figure 2) and other bands including radio, near-infrared and

<sup>2</sup> HEASOFT, the High Energy Astrophysics Software  
<https://www.swift.ac.uk/analysis/software.php>

<sup>3</sup> <https://heasarc.gsfc.nasa.gov/docs/heasarc/caldb/swift/>



X-ray bands (see [Hamsch et al. 2019](#), [Xu et al. 2019](#), [Bright et al. 2019](#) and [Hankins et al. 2019](#)).

## 4 OPTICAL SPECTRA

### 4.1 Spectral Evolution

Figure 3 shows the spectral evolution of MAXI J1820+070. The spectra are characterized by blue continua superimposed with  $H_\alpha$   $\lambda 6563$ ,  $H_\beta$   $\lambda 4861$ ,  $H_\gamma$   $\lambda 4341$ , He I  $\lambda 5876$ , He I  $\lambda 6678$ , He II  $\lambda 4686$  lines and Bowen blend. The detailed evolution of the main spectral features, i.e.,  $H_\alpha$ ,  $H_\beta$ ,  $H_\gamma$ , and He I  $\lambda 5876$  are shown in Figure 4. The profiles of these features all show some degrees of temporal evolution, with some having only a single Gaussian component while others showing asymmetric line profiles, or double-peaked emission, as shown in Figure 5. Using the Bayesian information criteria (BIC), a measure of the relative quality for a fit in model-selection ([Schwarz 1978](#)), we find that double Gaussian model (BIC=-548.8) works better than the single Gaussian model (BIC=-445.8) for  $H_\alpha$  line at some phases (i.e.,  $t=+39.78$  day). However, in other phases (i.e.,  $t=+113.63$  day), the amplitudes of two sub-components of double Gaussian model differ so greatly that the weaker component is negligible. In this case, the single Gaussian model is still a better fitting model for such profiles. The single/double-peaked profile transition of emission lines was previously reported in many BH X-ray binaries ([Fender et al. 2009](#); [Mata Sánchez et al. 2018](#)). A double-peaked line profile should originate from a rotating flow, i.e., the geometrically thin accretion discs ([Meyer 1986](#)), while winds from the accretion disc, driven by radiation pressure, tend to produce single-peaked lines ([Murray & Chiang 1996](#)). However, the asymmetric single-line profile in our spectra can be formed by double Gaussian components which blended due to lower spectral resolution. Adding to the complexity, an apparently double-peaked emission line can be also produced from an intrinsically single-peaked profile with a central absorption ([Fender et al. 2009](#)). Given the above uncertainties in applying the double gaussian fit, we thus adopted the single gaussian fit in the following analysis of the main spectral features.

### 4.2 Balmer Series

In Figure 6, we present the temporal evolution of parameters measured from the Balmer emission lines. The local pseudo-continuum is determined via a linear fit to both sides of the feature; and repeated visual inspections are required for reducing the noise ([Zhao et al. 2016](#)). The pEW is calculated with the equation below:

$$\text{pEW} = \int (F_o - F_c) / F_c d\lambda \quad (1)$$

where  $F_o$  is the observed flux and  $F_c$  is the flux of the local pseudo-continuum.

Note that the  $H_\alpha$  line shows a clear trend of strengthening within  $t \sim 300$  days from the initial detection of optical outburst, while its strength tends to decrease after  $t \sim 370$  days. The pEW of  $H_\beta$  line holds a similar evolutionary trend as  $H_\alpha$ . Such an evolution pattern in Balmer lines can be explained with the change in optical depth as discussed in

[Williams \(1980\)](#) and [Fender et al. \(2009\)](#). The spectrum of LMXB consists of a thermal continuum produced by inner hot, optically thick region of the disk, and emission lines formed in the outer cool region where the continuum is optically thin. During the rebrightening phase, the outer disc becomes hot as the X-ray irradiation gets stronger, and this makes the continuum become optically thick. The pEW of the emission lines depends on the relative size of the regions in the disk that are optically thin and thick in the continuum according to [Williams \(1980\)](#). Thus, the portion which is optically thick in the continuum increases during the rebrightening and this leads to decrease in pEW of optical lines from the outer region. The growth trend within  $\sim 300$  days can be also explained by this model. As the outer disk gets colder, an optically thin continuum forms at this stage and it leads to the increase in the pEWs of optical hydrogen emission lines.

To further examine the origin of the variation in  $H_\alpha$  emission, we show in Figure 7 the correlation between the pEW of  $H_\alpha$  and the  $r$ -band magnitude, which can characterize the strength of the continuum. The trend indicates that the pEW of  $H_\alpha$  emission increases when the system becomes faint in optical, and vice versa. It is consistent with the optical depth explanation of the evolution pattern in Balmer lines.

### 4.3 He I $\lambda 5876$ Feature

He I  $\lambda 5876$  is found to show persistent P-Cygni profiles in the spectra of MAXI J1820+070 taken during the X-ray low/hard state, as similarly reported by [Muñoz-Darias et al. \(2019\)](#). Similar P-Cygni profile was also seen in V404 Cygni and other BH LMXBs ([Mata Sánchez et al. 2018](#); [Casares et al. 2019](#)), where the continuous presence of P-Cygni profiles were proposed to result from an expanding outflow formed during the outburst. One can notice that there is a prominent absorption feature on the red side of He I  $\lambda 5876$ , which is likely due to the Galactic Na I D absorption doublet. The evolution of He I  $\lambda 5876$  emission line parameters is plotted in Figure 6, where one can see that the pEW follows a similar evolution trend as seen in  $H_\beta$ .

## 5 DISCUSSION

### 5.1 SED and Temperature

To examine the radiation characteristics of MAXI J1820+070, we constructed the spectral energy distribution (SED) with the *Swift*/UVOT, ground-based  $B$ ,  $g$ ,  $V$ ,  $r$ , and  $i$ -band photometry to derive the temperature and radius of the photosphere, as shown in Figure 8. During the outburst phases, the optical and UV emissions from the companion star are negligible compared to those from the accretion disc (and possibly jets). The corresponding SEDs, corrected for the galactic extinction, is shown in Figure 8. It can be seen that in general the SEDs can not be well described by a single blackbody model, with the deviations mostly coming from the UV bands. This suggests that the emission regions of the optical and UV bands have different temperatures, i.e., a multi-temperature disc. However, fitting to the optical and UV bands separately would not provide useful con-

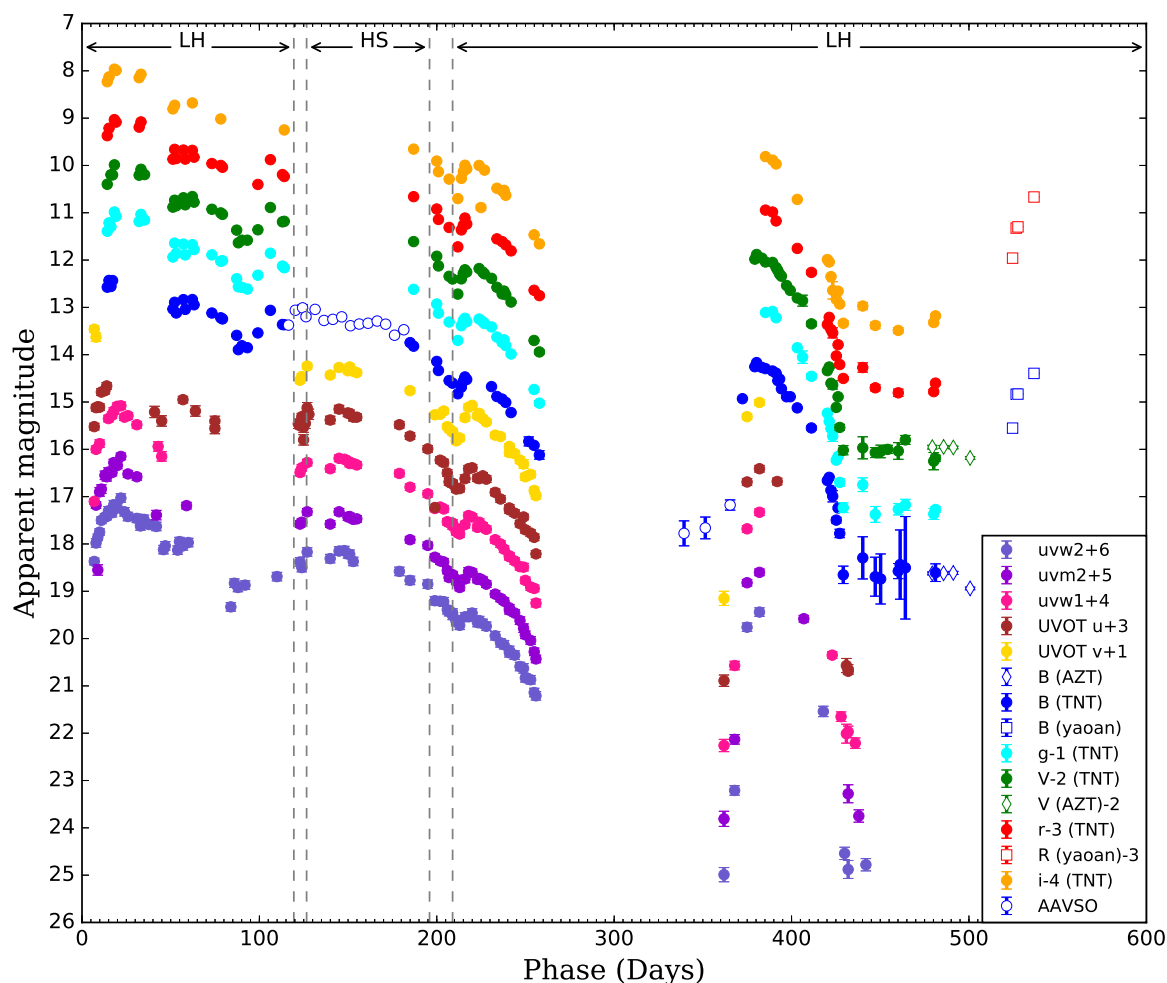


**Figure 2.** The optical and UV light curves obtained for MAXI J1820+070, lasting for about 550 days after the initial optical outburst (UT March 06.58 2018 = MJD 58184.08). Different colors represent different bands, including the *Swift* *uvw2*, *uvm2*, *uvw1*, UVOT *u*, UVOT *v*, *B*, *g*, *V*, *r*, *R*, *i*, and *I* bands. The light curves of different bands have been vertically shifted for better display. The arrow labels with ‘LH’ and ‘HS’ on the top represent the low/hard and high/soft state periods, respectively. The two narrow gaps between the LH and HS are intermediate-state periods (Shidatsu et al. 2019).

straints on different radiation zones because of limited data available for analysis. Contributions from the jets may also play a role, though they usually peak in the near-infrared bands (e.g., Corbel & Fender 2002; Russell et al. 2006).

Although the accretion disk may have multi-temperature components, the observed SED can still be reasonably fit by a simple blackbody model (Tucker et al. 2018), as shown in Figure 9. One can see that the blackbody temperature inferred from the multicolor photometry shows a rather complicated evolution, with an initial rapid increase from  $\sim 17,000$  K to  $23,000$  K, followed by a sudden drop to  $15,000$  K at  $t \sim 250$  days. After a possible plateau evolution during  $t \sim 100 - 200$  days, the temperature then suffered another dramatic decline, i.e. from  $15,000$  K at  $t \sim 250$  days to  $8,000$  K at  $t \sim 450$  days.

During the period from  $t \sim 15$  to  $\sim 80$  days after the initial outburst, MAXI J1820+070 appeared to become gradually hotter as its photosphere receded, which is consistent with the results from Tucker et al. (2018). From  $t \sim 180$  to  $\sim 260$  days, the optical and UV emission region cooled down. This is consistent with the Balmer series and He I emission lines becoming stronger during similar phases (see Section 4). After  $t \sim 380$  days, MAXI J1820+070 experienced a non-adiabatic evolution process, with the radiative radius becoming smaller while the temperature of the accretion disc keeping decreasing. Such a temperature decrease is consistent with the redwards evolution seen in the color curve (see Section 3 and Figure 10).

The  $B - V$ ,  $g - r$ , and  $r - i$  color curves of MAXI J1820+070, and the corresponding Spearman’s rank corre-

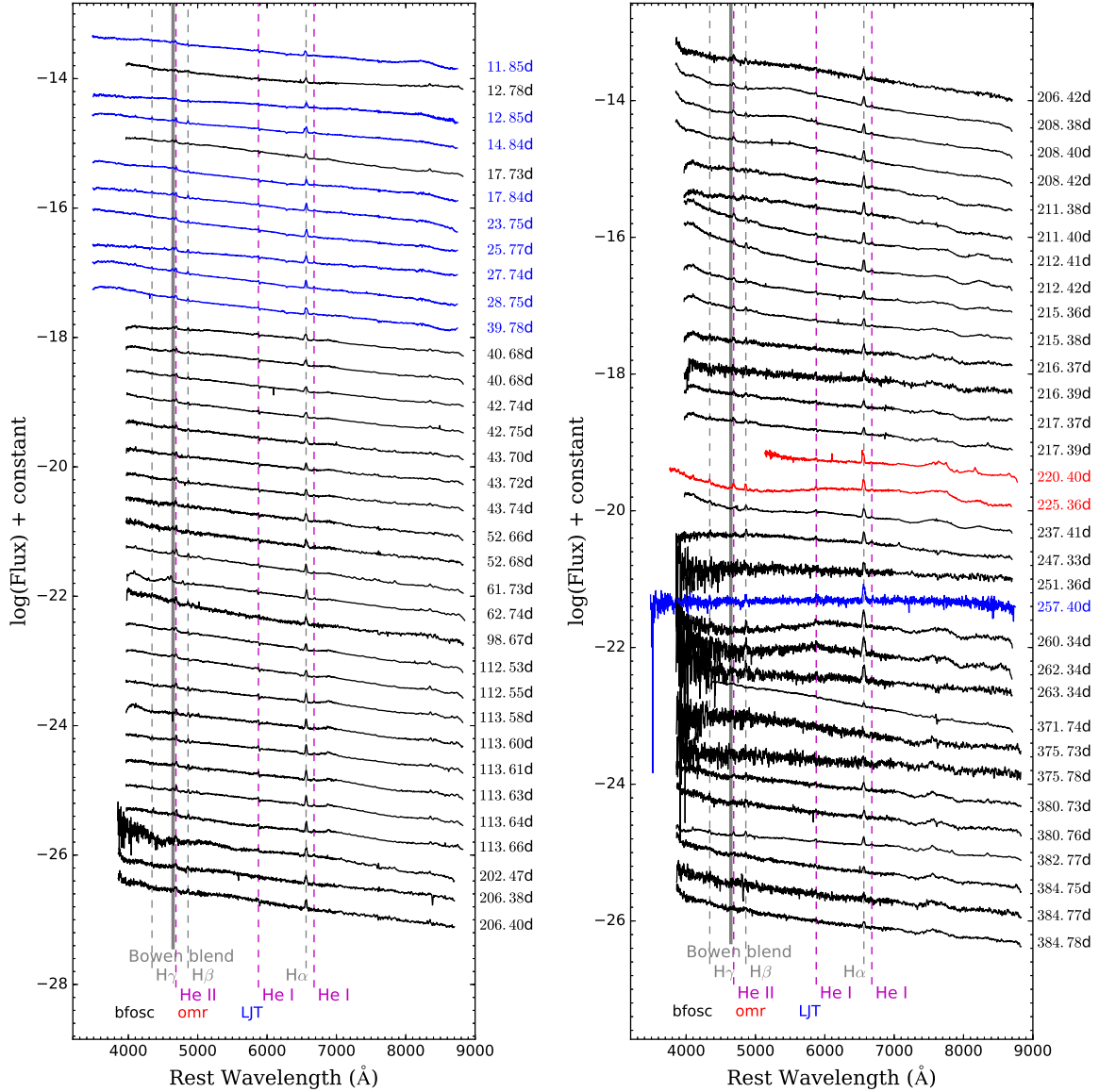


**Figure 3.** Spectral evolution of MAXI J1820+070. The continua of the spectra have been flux-calibrated by the photometry obtained at similar phases. The spectra have been shifted vertically for better display. The epoch on the right side of each spectrum represents the phase in days after the initial optical outburst. The Balmer series (including  $H_\alpha$ ,  $H_\beta$ , and  $H_\gamma$  here) and the helium emission lines are marked by grey and magenta dashed lines, respectively. The Bowen blend feature is labeled by the grey vertical bar in each panel. Different colors of the spectra represent different spectroscopic instruments (i.e., XLT+bfosc, XLT+omr or LJ+YFOSC), which are shown at the bottom of the plot.

lation coefficient with phases are shown in Figure 10. The positive correlations indicate the post-outburst color tends to become progressively redder with a statistical significance of  $\sim 4.5\sigma$ . This means the overall temperature of this system gradually decreased with time. However, the real physical process may be more complicated. There are some factors that cause the deviation from single blackbody, such as temperature difference in different regions of accretion disk and changes in optical depth.

## 5.2 Optical and X-ray Relation

As mentioned in Section 1, MAXI J1820+070 is very bright in both optical and X-ray bands during the outburst. This gives us an opportunity to study the correlation between emission features in optical and the X-ray luminosity and put constraints on the physics of BH accretion.

In Figure 11, we plot the pEW of  $H_\alpha$  emission as a function of X-ray luminosity inferred for MAXI J1820+070 at comparable phases. We adopted the average value for the pEW of  $H_\alpha$  line and X-ray luminosity when multiple obser-

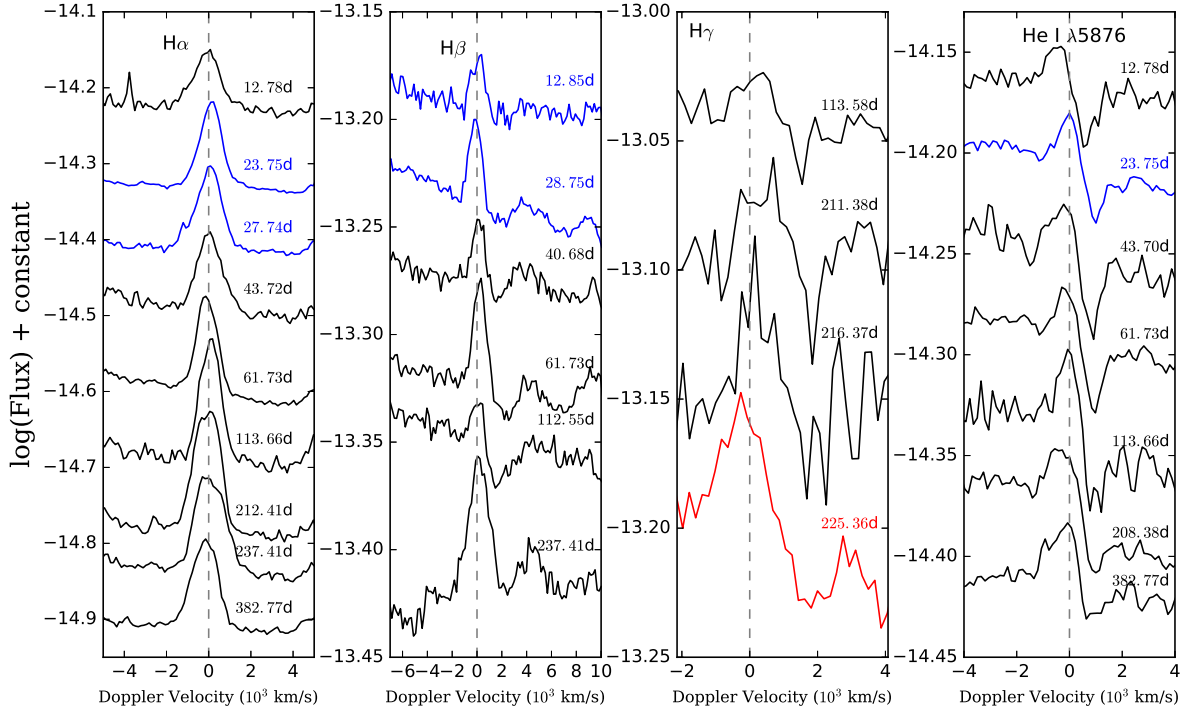


**Figure 4.** The  $H_{\alpha}$ ,  $H_{\beta}$ ,  $H_{\gamma}$ , and He I  $\lambda 5876$  lines of MAXI J1820+070 in velocity space. The colors represent the spectra obtained with the instruments marked in Figure 3.

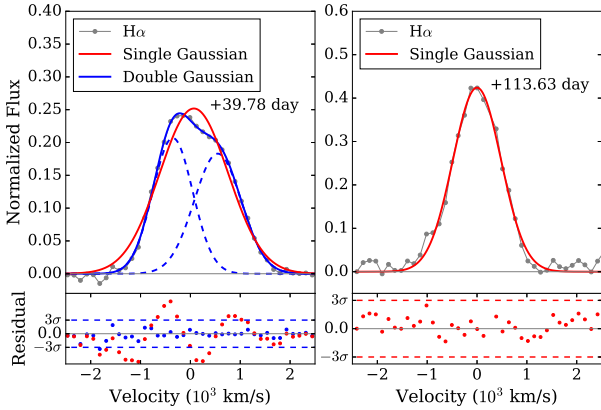


**Figure 5.** The  $H_{\alpha}$  line profile in two spectra of MAXI J1820+070, displayed in velocity space. Left panel: the  $H_{\alpha}$  line profile in the  $t = +39.78$  day spectrum. The red solid curve represents the fit curve using a single Gaussian function, while the blue solid line is the double Gaussian fit with two sub-components labeled by blue dashed lines. Right panel: the same case as in the left panel but for the  $t = +113.63$  day spectrum. The lower panels show the residuals of the observed line profiles relative to the best-fit profiles.

variations are available on the same day. For MAXI J1820+070, most of these observations were obtained in the low/hard states. An anticorrelation can be seen between X-ray lumi-

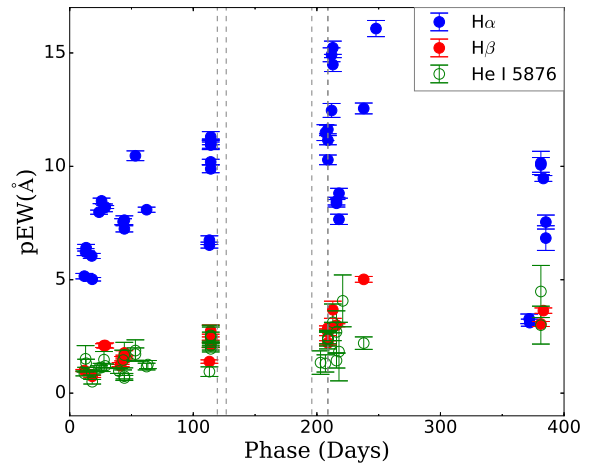


**Figure 6.** The pseudo equivalent width (pEW) evolution of the Balmer series and He I  $\lambda 5876$  in the spectra of MAXI J1820+070. All the lines were fit by single gaussian profiles. We use different colors to represent different spectral lines.

osity and the corresponding pEW of  $H_{\alpha}$  with a confidence level of 99.1% ( $2.64\sigma$ ). Based on a sample of six BH X-ray binaries, Fender et al. (2009) reported an anticorrelation between pEW of  $H_{\alpha}$  emission line and X-ray luminosity, which

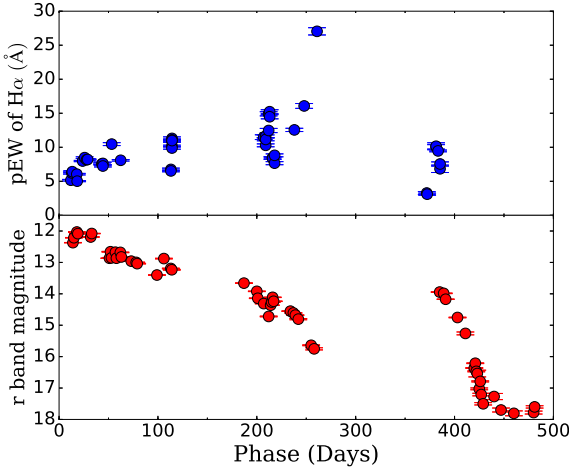


**Figure 7.** The pseudo equivalent width evolution of  $H_\alpha$  (top) and the  $r$ -band magnitude (bottom) measured for MAXI J1820+070. The time in days from the initial optical outburst are shown along the bottom axis.

is  $\text{pEW} \propto L_x^{-0.18 \pm 0.06}$ . Applying a power-law model to fit the observations of MAXI J1820+070, we get

$$\text{pEW} = 10^{4.3 \pm 1.1} L_x^{-0.092 \pm 0.030} \quad (2)$$

Note that this fit excludes the data point taken on  $t \sim +372$  days. Inspecting the X-ray and optical/UV light curves shown in Figure 12, one can see that at  $t \sim 372$  days, the optical and X-ray emission of MAXI J18020+070 was still in a rapid rising phase, and the BH binary system is likely in a transition state. This indicates that the anticorrelation between X-ray luminosity and  $H_\alpha$  emission holds in the outburst phase but not in the transition phase. Thus the radiation mechanisms of the lines and disks during the transition phase are not consistent with that of the post-outburst phase.

As the measured pEW suffered from the effect of continuum flux, we further examine the relations between the absolute flux of lines such as  $H_\alpha$ ,  $H_\beta$ , He II  $\lambda 4686$  and 2-10 keV X-ray flux, as shown in Figure 13. We find that the absolute fluxes of these lines show positive correlations with the X-ray radiation. We did not examine the correlation for He I  $\lambda 5876$  due to its possible blending with the Na I doublet. In comparison, the He II  $\lambda 4686$  line seems to show the strongest correlation with the X-ray flux, because He II has a higher ionization energy (i.e., 54.4 eV) and can only be excited by X-ray photons (Leloudas et al. 2019).

Because the FWHM of  $H_\beta$  and He II  $\lambda 4686$  lines can be used to determine the outer edge of the accretion disk, we further examined their correlations with X-ray emission in lower-panel of Figure 13. We found that with the increase of X-ray flux, both of these two lines tend to get weaker and then stabilize at  $1200 \text{ km s}^{-1}$  and  $1400 \text{ km s}^{-1}$ , respectively. Based on the fact that the gas motion in accretion disk can be approximated to follow the Kepler motion, its velocity can be determined by  $v = \sqrt{3/(8 \ln 2)}$  FWHM according to the analysis by Netzer (2013). The corresponding radius of the gas motion in the MAXI J1820+070 system can be estimated as  $1.71 \pm 0.13 R_\odot$  from  $H_\beta$  and  $1.25 \pm 0.11 R_\odot$  from

He II  $\lambda 4686$  line, respectively. We find that both of these two values are less than the typical radius of the accretion disk surrounding the stellar-mass BH (Lasota 2001), which equals to the 90% of effective Roche radius  $R_L = 2.46 R_\odot$ , identified by the relevant parameters obtained by Torres et al. (2019). The larger radius inferred from  $H_\beta$  relative to He II  $\lambda 4686$  indicates that the formation region of the former line can extend to the outer side of the accretion disk. This is due to the fact that He II  $\lambda 4686$  has a higher excitation energy than  $H_\beta$ . On the outer part of the accretion disk with lower temperature, only  $H_\beta$  can be excited. Note, however, that  $H_\alpha$  did not show such a similar relationship with X-ray flux. This suggests that the formation region of  $H_\alpha$  line was not confined to the accretion disk, but also included the outflow, as indicated by the P-cygni profile of  $H_\alpha$  from Muñoz-Darias et al. (2019).

The thermal-viscous DIM describes that, in quiescence, the accretion disk is filled up with matter, until at some radius, its temperature reaches the critical value that ionizes the hydrogen to trigger an outburst (Lasota 2001; Russell et al. 2019a). This outburst can be triggered within the inner part of the accretion disk, and then propagate outwards, which is called as “inside-out” outburst (Lasota 2001). However, in other LMXBs, the triggering process may start at the outer disc and then propagates inwards to the inner region, which is called as “outside-in” outburst (Shahbaz et al. 1998). Optical emission is usually produced by the outer disc, while the X-ray emission can be created on the viscous timescale when the inner disc is filled in. Thus detecting the time lag between different bands helps determine where the instability is triggered in the accretion disk.

Based on the method introduced in Tucker et al. (2018), we use a power-law function to fit the rising light curves,

$$\hat{F}_\lambda(t) = A \left( \frac{t - t_{0,\lambda}}{1 \text{ day}} \right)^B \quad (3)$$

where  $\hat{F}_\lambda$  is normalized flux for each band,  $t_{0,\lambda}$  is the zero point assumed for the reference epoch and  $t$  is the time of photometry. We focus on the time  $t_{0,0.1}$ , representing the epoch when the light curve reaches 1% of the peak flux. Tucker et al. (2018) found that during the initial outburst, the rising in optical preceded that in the X-ray by  $\Delta t = t_{0,0.1}^{B,AT} - t_{0,0.1}^{V,0.1} = 7.20 \pm 0.97$  days, and here we turn to study the time-lag during the rebrightening period from  $t \sim 370$  to 410 days. The power-law fits to the rebrightening evolution in  $B$  band and *Swift* XRT 2-10 keV band are plotted in the inset of Figure 12. Based on the fitting parameters and bootstrap-resampling technique of estimating errors, we get  $t_{0,0.1}^{X,RT} = 58.92 \pm 0.15$  days for *Swift* XRT (2-10 keV) and  $t_{0,0.1}^B = 38.12 \pm 2.70$  days for the  $B$  band. Then we can determine a time lag between optical and X-ray outbursts as  $\Delta t = t_{0,0.1}^{X,RT} - t_{0,0.1}^B = 20.80 \pm 2.85$  ( $\Delta t \pm 2\sigma$ ) days. This means that during the rebrightening process, the start of the rising in optical preceded that in the X-ray, which is consistent with the estimate for the first outburst from Tucker et al. (2018). The time-lag allows constraints on the radius  $R(B)$  for the disk where the outburst is triggered and propagates simultaneously both inward and outward until reaching the inner region and producing the X-rays. We use the scaling relation in Bernardini et al. (2016) and the same parameter setup adopted in Tucker et al. (2018) to find the radius as  $R(B) = [0.025 - 0.079] R_\odot$  ( $2\sigma$ ), which for the initial out-



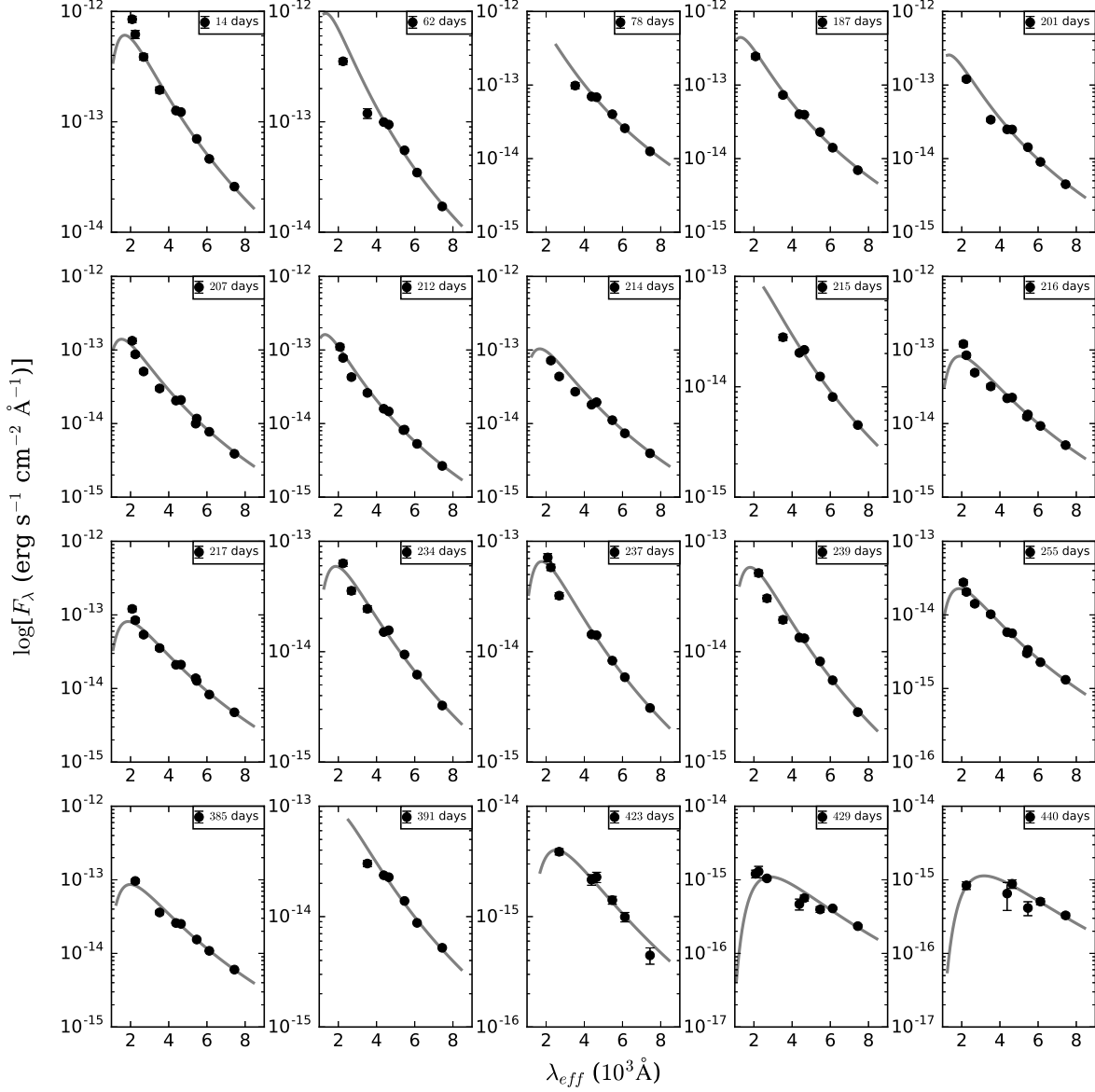


**Figure 8.** Fits to the SEDs of MAXI J1820+070 using a single blackbody model. Data points are presented in filled circles and the grey lines show the best-fit models.

burst is  $R(V) = [0.01 - 0.04]R_{\odot}$ , approval of the DIM and irradiation models for BH LMXB.

For MAXI J1820+070, one interesting evolution occurred at  $t \sim 200$  to 300 days, when the emission is found to show much larger decrease in X-ray than in optical and UV bands (see also Figure 12). This observation fact suggests that the effects of irradiation on the accretion disk are diminishing during this phase, and the viscous energy of the accretion disk may contribute to maintain a lower rate of decline. Moreover, in MAXI J1820+070, an intensity jump

appears in optical and UV bands at  $t \sim 210$  days. [Augusteijn et al. \(1993\)](#) reported that some LMXBs exhibited intensity jumps during the decay of the initial outburst, and they interpreted this phenomenon as an instantaneous response of the companion to the heating of X-rays and a response of the disk to the extra mass flow. The amplitude of this intensity jump tends to get stronger in redder bands (and vice versa). Note, however, this intensity jump did not occur in the X-ray band. This can be explained by a temporary increase in accretion rate of the outer disk, while this change

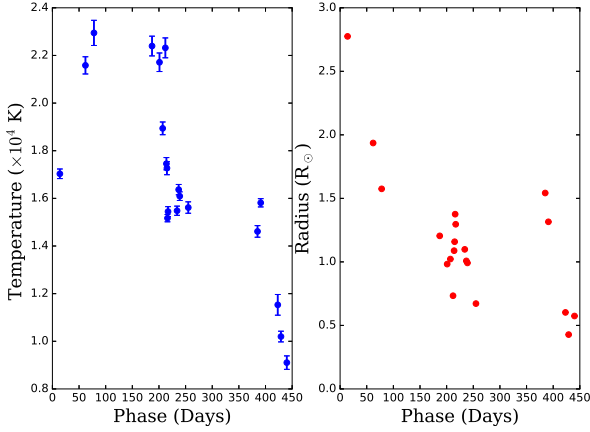


**Figure 9.** Evolution of temperature (left) and radius (right) inferred for MAXI J1820+070 from the blackbody fits. The blue and red dots are the best-fit values of temperature and radius, respectively.

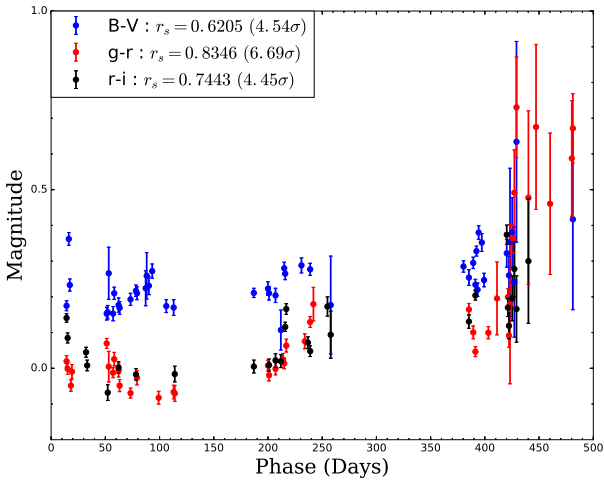


**Figure 10.** The  $B - V$ ,  $g - r$ , and  $r - i$  color evolution of MAXI J1820+070.  $r_s$  in the inset window represents the coefficient of the Spearman's correlation between the color evolution and the phase, while the number in the bracket represents the significance level.

will not affect the inner disk due to a longer viscous time scale.

## 6 CONCLUSIONS

In this work, we present optical, UV and X-ray observations and studies for the BH binary system MAXI J1820+070. Several outbursts/rebrightenings were recorded during our monitoring campaign spanning from its initial optical outburst to  $\sim 550$  days after. The main results from our analysis of the data are summarized as follows.

- (i) The spectra of MAXI J1820+070 are characterized by

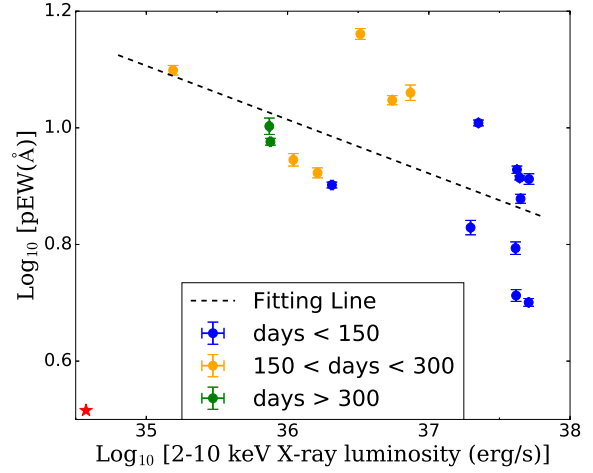


**Figure 11.** Relation between the  $H_\alpha$  pEW measured with the spectra presented in this paper and the X-ray luminosity inferred from the *Swift* observations (2-10 keV). All the data are included in our fitting except the red star at the bottom left corner. Different colors represent different phases.

blue continuum and the superimposed Balmer series, helium emission lines, and Bowen blend features, similar to those seen in several other well-known BH LMXBs like V404 Cygni (Mata Sánchez et al. 2018). The  $H_\alpha$  emission becomes progressively strong within  $\sim 300$  days from the first detection of outburst, followed by a subsequent weakening during 350–400 days. A similar trend can be also found in the  $H_\beta$  feature. The  $\text{He I } \lambda 5876$  line is also found to become progressively stronger during the phase from the first detection to about 400 days after that. Such an evolution trend can be explained by the change in optical depth of continuum, as a result of the temperature change of the outer disc during the outburst.

(ii) Based on extensive optical spectroscopy and the X-ray observations of MAXI J1820+070, we analyzed the relationship between the X-ray luminosity and the pEW of the  $H_\alpha$  emission, and we found an anticorrelation as  $\text{pEW}_{H_\alpha} = 10^{4.3 \pm 1.1} L_x^{-0.092 \pm 0.030}$ , confirming previous results.

(iii) After removing the effect of continuum, the absolute flux of  $H_\alpha$ ,  $H_\beta$  and  $\text{He II } \lambda 4686$  showed positive correlations with the X-ray flux obtained at similar phases. This confirms that the high-energy irradiation can be regarded the pumping source for the emission of MAXI1820+070. In addition, the FWHM of  $H_\beta$  and  $\text{He II } \lambda 4686$  is found to become smaller with the increase of X-ray flux but they tend to stabilize at line forming region of  $1.25 - 1.71 R_\odot$ , consistent with the typical radius of accretion disk around a stellar-size black hole.

(iv) The time lag found for the change in emission between optical and X-ray bands is  $\Delta t = t_{0.01}^{XRT} - t_{0.01}^B = 20.80 \pm 2.85$  ( $\Delta t \pm 2\sigma$ ) days, which means that during the rebrightening process, the start of the rising in optical preceded that in the X-ray.

(v) At  $t \sim 200$ –300 days, the X-ray flux is found to show a sudden drop, while the flux variation in optical/UV flux is

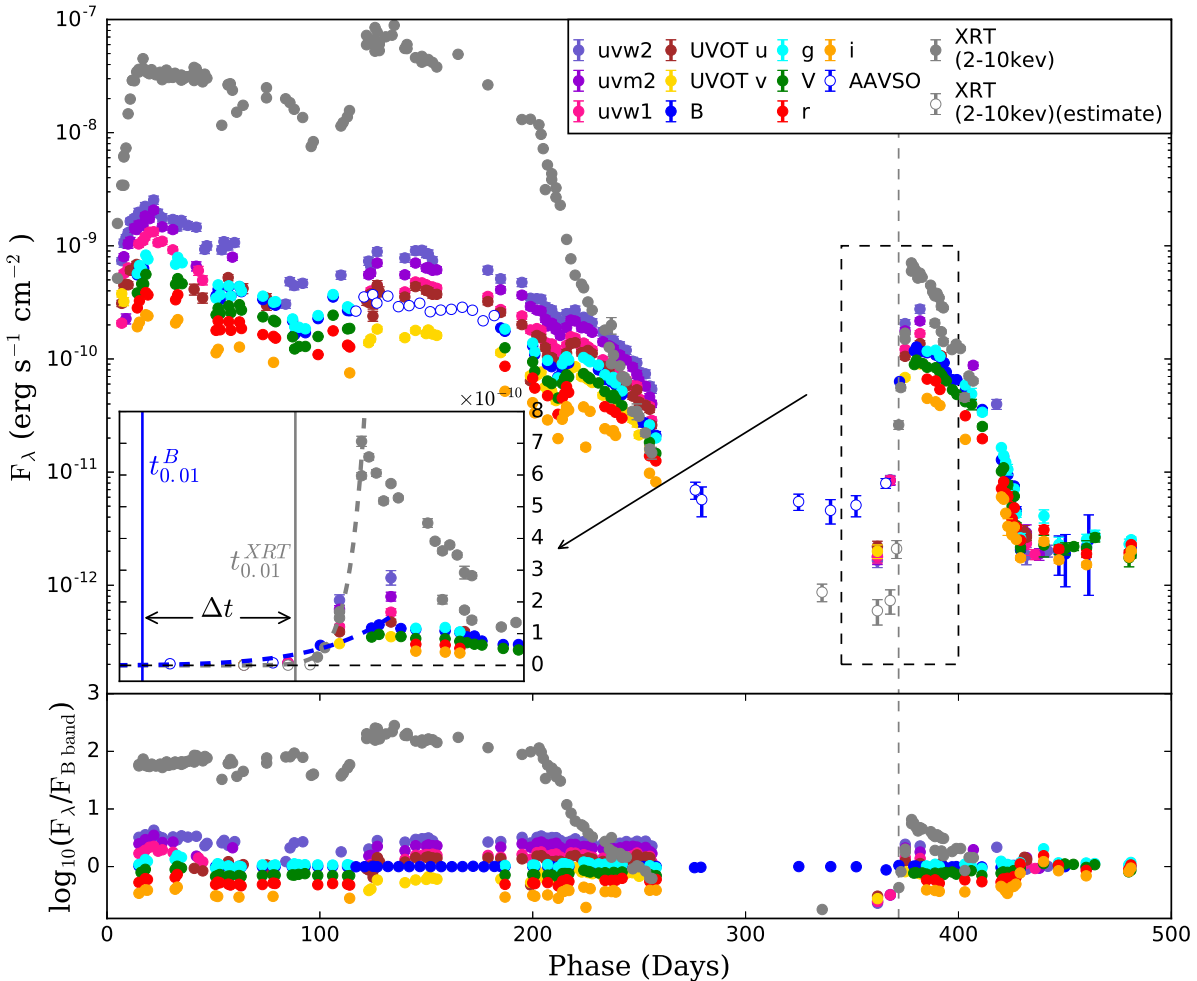


**Figure 12.** The upper panel shows the optical, UV and X-ray light curves of MAXI J1820+070, which are all converted into flux, while the lower panel shows the logarithmic ratio of flux in each band to the flux in B band. Different colors represent different bands, including XRT (2-10keV), *uvw2*, *uvm2*, *uvw1*, UVOT *u*, UVOT *v*, *B*, *g*, *V*, *r*, and *i* bands, as shown in the legend. The phase is defined in the same way as in Figure 2. The epoch of data represented by a red star in Figure 11 is marked by grey dashed line and the specific light curve around this time (345 - 400 days) is shown in the inset. The power-law fits to the rising light curves for XRT (2-10keV) and *B* bands are shown in dashed lines with corresponding colors. The values of  $t_{0.01}$  and the time lag ( $\Delta t$ ) measured for the rebrightening between *B* band and XRT (2-10keV), are also shown.

much less significant. This discrepancy suggests that the viscous energy of the accretion disk can contribute significantly to the optical/UV flux when irradiation diminished.

## ACKNOWLEDGEMENTS

We thank the anonymous referee for suggestive comments to help improve this work. We acknowledge the support of the staff of the Lijiang 2.4 m and Xinglong 2.16 m telescopes. Funding for the LJT has been provided by Chinese Academy of Sciences and the People's Government of Yunnan Province. The LJT is jointly operated and administered by Yunnan Observatories and the Center for As-

tronomical Mega-Science, CAS. We acknowledge the support of the staff of the Xinglong 80cm telescope. It was partially supported by the Open Project Program of the Key Laboratory of Optical Astronomy, National Astronomical Observatories, Chinese Academy of Sciences. This work is supported by the National Natural Science Foundation of China (NSFC grants 12033003, 11761141001 and 11633002), the National Program on Key Research and Development Project (grant no. 2016YFA0400803). X.W. is also supported by the Scholar Program of Beijing Academy of Science and Technology (BS2020002). J.W. acknowledges the support of the National Natural Science Foundation of China (grant No. U1938105) and the President Fund of Xi-

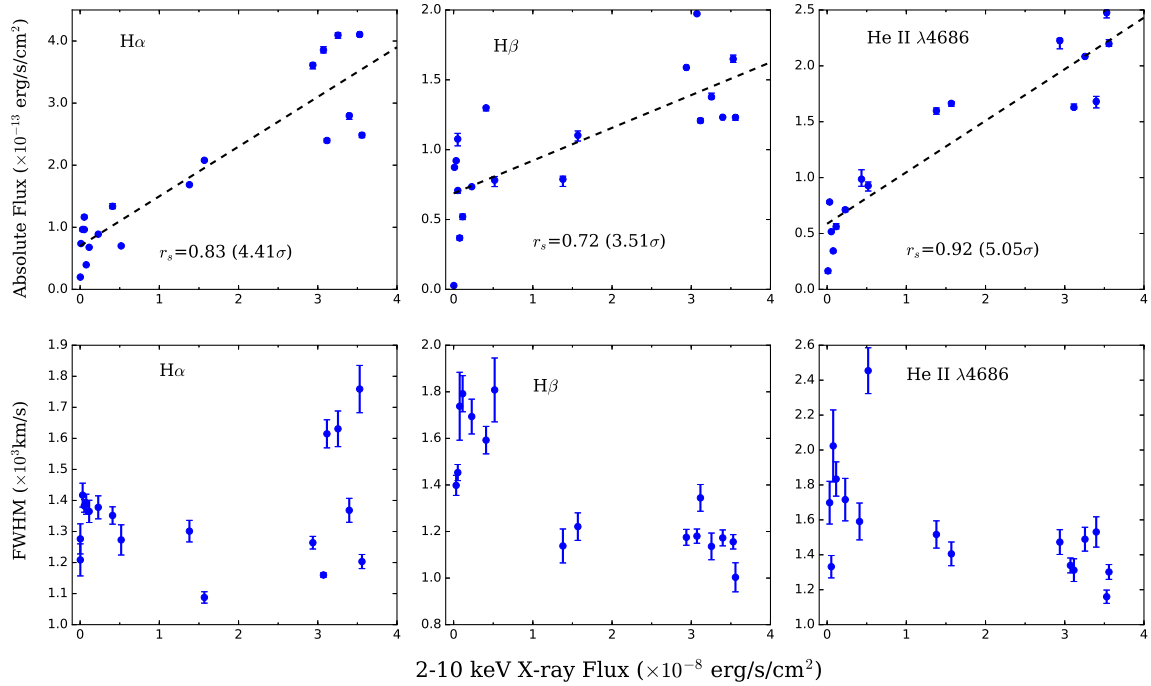


**Figure 13.** Top panel: The relation between 2-10 keV X-ray flux and the absolute flux of  $H\alpha$ ,  $H\beta$  and  $He\ II\ \lambda 4686$ . The black dashed lines in above three panels represent the best linear fit to the data. The results of Spearman's rank correlation test was labeled in each panel. Bottom panel: The relation between 2-10 keV X-ray flux and the FWHM of  $H\alpha$ ,  $H\beta$  and  $He\ II\ \lambda 4686$  lines.

amen University (No. 20720190051). Lingzhi Wang is sponsored (in part) by the Chinese Academy of Sciences (CAS), through a grant to the CAS South America Center for Astronomy (CASSACA) in Santiago, Chile. CYW is supported by the National Natural Science Foundation of China (NSFC grants 12003013). This research has made use of data provided by the Yaoan High Precision Telescope. We thank the staff of AZT for their observations and allowance of the use of the data. We acknowledge with thanks the variable star observations from the AAVSO International Database contributed by observers worldwide and used in this research.

*software:* ZrutyPhot (Mo et al. in prep.), IRAF (Tody 1986, 1993), SExtractor (Bertin & Arnouts 1996)

## DATA AVAILABILITY

The data underlying this article are available in the article. Our photometric data has been attached in Table A1, A2 and A3 in the appendix. The log table of spectral data is also shown in Table A4.

## REFERENCES

Atri P., et al., 2020, *MNRAS*, **493**, L81  
 Augusteijn T., Kuulkers E., Shaham J., 1993, *A&A*, **279**, L13  
 Baglio M. C., Russell D. M., Lewis F., 2018, The Astronomer's Telegram, **11418**, 1

Bahramian A., Motta S., Atri P., Miller-Jones J., 2019, The Astronomer's Telegram, **12573**  
 Bernardini F., Russell D. M., Shaw A. W., Lewis F., Charles P. A., Koljonen K. I. I., Lasota J. P., Casares J., 2016, *ApJ*, **818**, L5  
 Bertin E., Arnouts S., 1996, *A&AS*, **117**, 393  
 Bright J., Motta S., Williams D., Fender R., Woudt P., Miller-Jones J., 2019, The Astronomer's Telegram, **13041**, 1  
 Casares J., Jonker P. G., 2014, *Space Sci. Rev.*, **183**, 223  
 Casares J., Muñoz-Darias T., Mata Sánchez D., Charles P. A., Torres M. A. P., Armas Padilla M., Fender R. P., García-Rojas J., 2019, *MNRAS*, **488**, 1356  
 Charles P. A., Coe M. J., 2006, Optical, ultraviolet and infrared observations of X-ray binaries. pp 215–265  
 Chen W., Shrader C. R., Livio M., 1997, *ApJ*, **491**, 312  
 Corbel S., Fender R. P., 2002, *ApJ*, **573**, L35  
 Dubus G., Hameury J. M., Lasota J. P., 2001, *A&A*, **373**, 251  
 Ehgamberdiev S., 2018, *Nature Astronomy*, **2**, 349  
 Eikenberry S. S., Matthews K., Murphy Jr. T. W., Nelson R. W., Morgan E. H., Remillard R. A., Munro M., 1998, *ApJ*, **506**, L31  
 Fender R. P., Russell D. M., Knigge C., Soria R., Hynes R. I., Goad M., 2009, *MNRAS*, **393**, 1608  
 Fukugita M., Ichikawa T., Gunn J. E., Doi M., Shimasaku K., Schneider D. P., 1996, *AJ*, **111**, 1748  
 Gandhi P., Rao A., Johnson M. A. C., Paice J. A., Maccarone T. J., 2019, *MNRAS*, **485**, 2642  
 Gehrels N., et al., 2004, *ApJ*, **611**, 1005  
 Gierliński M., Done C., Page K., 2008, *MNRAS*, **388**, 753  
 Gierliński M., Done C., Page K., 2009, *MNRAS*, **392**, 1106  
 Gu W.-M., et al., 2019, *ApJ*, **872**, L20  
 Hamsch J., Ulwetz J., Vanmunster T., Cejudo D., Patterson J., 2019, The Astronomer's Telegram, **13014**, 1



Hankins M., et al., 2019, The Astronomer’s Telegram, [13044](#), 1

Homan J., et al., 2018, The Astronomer’s Telegram, [11820](#), 1

Huang F., Li J.-Z., Wang X.-F., Shang R.-C., Zhang T.-M., Hu J.-Y., Qiu Y.-L., Jiang X.-J., 2012, [Research in Astronomy and Astrophysics](#), **12**, 1585

Johnson H. L., Mitchell R. I., Iriarte B., Wisniewski W. Z., 1966, Communications of the Lunar and Planetary Laboratory, **4**, 99

Kawamuro T., et al., 2018, The Astronomer’s Telegram, [11399](#), 1

Kirsch M. G., et al., 2005, Crab: the standard x-ray candle with all (modern) x-ray satellites. pp 22–33, [doi:10.1117/12.616893](#)

Kochanek C. S., et al., 2017, [PASP](#), **129**, 104502

Lasota J.-P., 2001, [New Astron. Rev.](#), **45**, 449

Leloudas G., et al., 2019, [ApJ](#), **887**, 218

Lin J., Yan Z., Han Z., Yu W., 2019, [ApJ](#), **870**, 126

Markoff S., Nowak M. A., Wilms J., 2005, [ApJ](#), **635**, 1203

Mata Sánchez D., et al., 2018, [MNRAS](#), **481**, 2646

Matsuoka M., et al., 2009, [PASJ](#), **61**, 999

Meyer F., 1986, [MNRAS](#), **218**, 7P

Mihara T., et al., 2011, [PASJ](#), **63**, S623

Muñoz-Darias T., et al., 2019, [ApJ](#), **879**, L4

Murray N., Chiang J., 1996, [Nature](#), **382**, 789

Netzer H., 2013, The Physics and Evolution of Active Galactic Nuclei. Cambridge University Press, [doi:10.1017/CBO9781139109291](#)

Osaki Y., 1995, [PASJ](#), **47**, 47

Remillard R. A., McClintock J. E., 2006, [ARA&A](#), **44**, 49

Roming P. W. A., et al., 2005, [Space Sci. Rev.](#), **120**, 95

Russell D. M., Fender R. P., Hynes R. I., Brocksopp C., Homan J., Jonker P. G., Buxton M. M., 2006, [MNRAS](#), **371**, 1334

Russell D. M., et al., 2019a, [Astronomische Nachrichten](#), **340**, 278

Russell D. M., Baglio M. C., Lewis F., 2019b, The Astronomer’s Telegram, [12534](#)

Rykoff E. S., Miller J. M., Steeghs D., Torres M. A. P., 2007, [ApJ](#), **666**, 1129

Schwarz G., 1978, [The Annals of Statistics](#), **6**, 461

Shahbaz T., Bandyopadhyay R. M., Charles P. A., Wagner R. M., Muhli P., Hakala P., Casares J., Greenhill J., 1998, [MNRAS](#), **300**, 1035

Shappee B. J., et al., 2014, [ApJ](#), **788**, 48

Shidatsu M., Nakahira S., Murata K. L., Adachi R., Kawai N., Ueda Y., Negoro H., 2019, [ApJ](#), **874**, 183

Tody D., 1986, The IRAF Data Reduction and Analysis System. p. 733, [doi:10.1117/12.968154](#)

Tody D., 1993, IRAF in the Nineties. p. 173

Tomsick J. A., Homan J., 2019, The Astronomer’s Telegram, [12732](#)

Torres M. A. P., Casares J., Jiménez-Ibarra F., Muñoz-Darias T., Armas Padilla M., Jonker P. G., Heida M., 2019, [ApJ](#), **882**, L21

Tucker M. A., et al., 2018, [ApJ](#), **867**, L9

Ulowetz J., Myers G., Patterson J., 2019, The Astronomer’s Telegram, [12567](#)

Veledina A., et al., 2019, [A&A](#), **623**, A75

Vozza D., Ali S., Balakrishnan M., Chen J., Kebebe N., Miller J. M., Reynolds M., Tetarenko B. E., 2019, The Astronomer’s Telegram, [12688](#)

Williams R. E., 1980, [ApJ](#), **235**, 939

Wu K., Soria R., Hunstead R. W., Johnston H. M., 2001, [MNRAS](#), **320**, 177

Wu K., Soria R., Johnston H., Hunstead R., 2002, in Gurzadyan V. G., Jantzen R. T., Ruffini R., eds, The Ninth Marcel Grossmann Meeting. pp 2274–2275 ([arXiv:astro-ph/0101390](#)), [doi:10.1142/9789812777386\\_0550](#)

Wu J., et al., 2015, [ApJ](#), **806**, 92

Wu J., Orosz J. A., McClintock J. E., Hasan I., Bailyn C. D., Gou L., Chen Z., 2016, [ApJ](#), **825**, 46

Xu Y., Harrison F., Tomsick J., 2019, The Astronomer’s Telegram, [13025](#), 1

Zhang J.-C., Fan Z., Yan J.-Z., Bharat Kumar Y., Li H.-B., Gao D.-Y., Jiang X.-J., 2016, [PASP](#), **128**, 105004

Zhao X., et al., 2016, [ApJ](#), **826**, 211

van Paradijs J., McClintock J. E., 1994, [A&A](#), **290**, 133

## APPENDIX A: PHOTOMETRIC AND SPECTROSCOPIC DATA

This paper has been typeset from a  $\text{\LaTeX}$  file prepared by the author.

**Table A1.** Photometric Standards in the MAXI J1820+070 Field

Num.	$\alpha$ (J2000)	$\delta$ (J2000)	$B$ (mag)	$V$ (mag)	$g$ (mag)	$r$ (mag)	$i$ (mag)
1	18 <sup>h</sup> 20 <sup>m</sup> 25 <sup>s</sup> .4256	7°09'21".6576	14.524(068)	13.828(032)	14.081(002)	13.647(001)	13.437(001)
2	18 <sup>h</sup> 20 <sup>m</sup> 32 <sup>s</sup> .2418	7°15'02".0196	14.534(091)	13.862(037)	14.111(006)	13.701(005)	13.542(003)
3	18 <sup>h</sup> 20 <sup>m</sup> 40 <sup>s</sup> .1472	7°10'57".8100	15.361(090)	13.808(033)	14.419(001)	13.667(030)	12.982(...)
4	18 <sup>h</sup> 20 <sup>m</sup> 26 <sup>s</sup> .4202	7°10'11".7948	13.976(095)	12.796(046)	...	...	...
5	18 <sup>h</sup> 20 <sup>m</sup> 27 <sup>s</sup> .5782	7°11'40".8696	14.697(101)	13.622(039)	...	...	...
6	18 <sup>h</sup> 20 <sup>m</sup> 25 <sup>s</sup> .6668	7°15'51".2424	14.037(101)	12.805(044)	...	...	...
7	18 <sup>h</sup> 20 <sup>m</sup> 40 <sup>s</sup> .0294	7°12'01".9044	14.778(091)	13.322(036)	...	...	...
8	18 <sup>h</sup> 20 <sup>m</sup> 31 <sup>s</sup> .2221	7°06'48".8412	13.792(077)	12.285(030)	...	...	...
9	18 <sup>h</sup> 20 <sup>m</sup> 07 <sup>s</sup> .1098	7°13'28".6068	14.909(096)	14.286(045)	...	...	...
10	18 <sup>h</sup> 20 <sup>m</sup> 10 <sup>s</sup> .1870	7°13'50".7982	...	...	14.759(002)	14.189(002)	13.960(001)
11	18 <sup>h</sup> 20 <sup>m</sup> 32 <sup>s</sup> .1594	7°07'04".6632	...	...	14.760(002)	14.201(001)	13.975(000)
12	18 <sup>h</sup> 20 <sup>m</sup> 18 <sup>s</sup> .5156	7°10'32".7939	...	...	14.851(003)	14.051(001)	13.687(005)

Note: Uncertainties, in units of 0.001 mag, are  $1\sigma$ .

**Table A2.** Ground-based Optical Photometry of MAXI J1820+070

MJD	Phase <sup>a</sup>	<i>B</i> (mag)	<i>g</i> (mag)	<i>V</i> (mag)	<i>r</i> (mag)	<i>R</i> (mag)	<i>i</i> (mag)	data source
58198.3	14.2	12.573(005)	12.390(010)	12.398(009)	12.371(006)	...	12.230(006)	TNT
58199.3	15.2	12.430(008)	12.212(008)	...	12.214(008)	...	12.129(006)	TNT
58200.4	16.3	12.558(012)	12.294(014)	12.196(006)	...	...	...	TNT
58201.3	17.2	12.433(007)	...	12.200(010)	...	...	...	TNT
58202.3	18.2	...	11.983(007)	...	12.032(009)	...	11.965(010)	TNT
58202.4	18.3	...	...	11.987(007)	...	...	...	TNT
58203.3	19.2	...	12.074(010)	...	12.084(010)	...	11.991(009)	TNT
58216.3	32.2	...	12.185(006)	12.206(007)	12.191(009)	...	12.146(005)	TNT
58217.3	33.2	...	12.034(006)	12.081(005)	12.080(006)	...	12.072(009)	TNT
58219.4	35.3	...	12.153(007)	12.193(008)	...	...	...	TNT
58235.3	51.2	13.034(008)	12.936(007)	12.881(010)	12.867(007)	...	12.805(008)	TNT
58236.3	52.2	12.892(011)	12.641(011)	12.735(008)	12.660(011)	...	12.728(011)	TNT
58237.2	53.1	13.118(040)	12.858(030)	12.852(033)	12.854(013)	...	...	TNT
58241.2	57.1	12.836(012)	12.662(007)	12.683(008)	12.675(007)	...	...	TNT
58242.3	58.2	13.042(009)	12.891(008)	12.832(008)	12.866(011)	...	...	TNT
58246.3	62.2	12.834(011)	12.674(009)	12.657(009)	12.681(009)	...	12.679(007)	TNT
58247.2	63.1	12.945(011)	12.777(010)	12.776(007)	12.826(007)	...	...	TNT
58257.3	73.2	13.119(010)	12.890(007)	12.926(007)	12.960(007)	...	...	TNT
58262.3	78.2	13.220(009)	13.025(008)	13.003(007)	13.000(009)	...	13.017(007)	TNT
58263.3	79.2	13.244(010)	13.012(011)	13.034(008)	13.039(009)	...	...	TNT
58271.3	87.2	13.591(028)	13.394(019)	13.367(021)	...	...	...	TNT
58272.2	88.1	13.894(036)	13.565(025)	13.635(029)	...	...	...	TNT
58274.2	90.1	13.811(013)	13.578(008)	13.580(012)	...	...	...	TNT
58277.3	93.2	13.852(011)	13.612(010)	13.580(009)	...	...	...	TNT
58283.2	99.1	13.540(008)	13.319(009)	13.360(007)	13.402(009)	...	...	TNT
58290.3	106.2	13.063(007)	12.855(007)	12.889(011)	12.878(010)	...	...	TNT
58297.1	113.0	13.362(012)	13.126(009)	13.192(010)	13.193(010)	...	...	TNT
58298.1	114.0	13.366(013)	13.163(010)	13.181(011)	13.234(012)	...	13.250(010)	TNT
58300.5	116.4	13.374(010)	...	...	...	...	...	AAVSO
58304.3	120.2	13.061(011)	...	...	...	...	...	AAVSO
58308.4	124.3	13.010(065)	...	...	...	...	...	AAVSO
58310.4	126.3	13.197(045)	...	...	...	...	...	AAVSO
58315.5	131.4	13.042(007)	...	...	...	...	...	AAVSO
58320.5	136.4	13.276(009)	...	...	...	...	...	AAVSO
58325.5	141.4	13.253(009)	...	...	...	...	...	AAVSO
58330.5	146.4	13.200(014)	...	...	...	...	...	AAVSO
58335.4	151.3	13.388(028)	...	...	...	...	...	AAVSO
58340.4	156.3	13.352(026)	...	...	...	...	...	AAVSO
58345.3	161.2	13.335(013)	...	...	...	...	...	AAVSO
58350.5	166.4	13.289(010)	...	...	...	...	...	AAVSO
58355.3	171.2	13.355(017)	...	...	...	...	...	AAVSO
58360.3	176.2	13.588(014)	...	...	...	...	...	AAVSO
58365.5	181.4	13.473(012)	...	...	...	...	...	AAVSO
58369.0	184.9	13.745(008)	...	...	...	...	...	TNT
58371.0	186.9	13.820(006)	13.618(007)	13.609(007)	13.660(010)	...	13.655(008)	TNT
58384.0	199.9	14.142(008)	13.928(007)	13.919(011)	13.921(008)	...	...	TNT
58384.1	200.0	...	...	...	...	...	13.907(010)	TNT
58385.0	200.9	14.334(008)	14.122(007)	14.124(011)	14.142(009)	...	14.133(008)	TNT
58391.0	206.9	14.547(010)	14.309(008)	14.343(010)	14.311(009)	...	14.289(010)	TNT
58393.0	208.9	14.602(010)	...	14.400(006)	...	...	...	TNT
58395.9	211.8	14.826(037)	14.698(013)	14.719(019)	...	...	...	TNT
58396.0	211.9	...	...	...	14.721(011)	...	14.701(007)	TNT
58397.9	213.8	14.687(030)	14.387(008)	14.397(010)	14.363(009)	...	...	TNT
58398.0	213.9	...	...	...	...	...	14.274(010)	TNT
58399.0	214.9	14.560(010)	14.276(006)	14.280(007)	14.263(009)	...	...	TNT
58399.1	215.0	...	...	...	...	...	14.129(010)	TNT
58400.0	215.9	14.470(010)	14.230(007)	14.205(007)	14.112(007)	...	13.996(006)	TNT
58401.0	216.9	14.523(010)	14.301(010)	14.253(010)	14.238(008)	...	14.072(007)	TNT
58408.0	223.9	...	14.246(007)	14.179(007)	...	...	14.000(007)	TNT
58409.0	224.9	...	...	...	...	...	14.890(054)	TNT
58410.0	225.9	...	14.302(008)	14.254(009)	...	...	...	TNT
58411.0	226.9	...	14.340(008)	14.291(008)	...	...	14.099(008)	TNT

<sup>a</sup> Days relative to the initial optical outburst (UT March 06.58 2018 = MJD 58184.08).Note: Uncertainties, in units of 0.001 mag, are 1 $\sigma$ .

**Table A2** – *continued* A table continued from the previous one.

MJD	Phase <sup>a</sup>	<i>B</i> (mag)	<i>g</i> (mag)	<i>V</i> (mag)	<i>r</i> (mag)	<i>R</i> (mag)	<i>i</i> (mag)	data source
58415.0	230.9	14.674(012)	14.413(008)	14.386(009)	...	...	...	TNT
58418.0	233.9	14.883(010)	14.627(011)	14.575(011)	14.552(010)	...	14.482(010)	TNT
58420.9	236.8	14.938(026)	14.739(011)	14.715(011)	14.610(009)	...	14.538(007)	TNT
58422.0	237.9	...	14.685(009)	14.655(009)	...	...	14.526(011)	TNT
58423.0	238.9	15.009(009)	14.808(007)	14.732(008)	14.679(008)	...	14.631(007)	TNT
58426.0	241.9	15.223(030)	14.985(027)	14.887(025)	14.806(020)	...	...	TNT
58436.0	251.9	15.833(095)	...	...	...	...	...	TNT
58438.9	254.8	15.916(029)	15.735(014)	15.699(015)	15.639(013)	...	15.466(014)	TNT
58441.9	257.8	16.119(090)	16.024(056)	15.942(047)	15.752(034)	...	15.658(032)	TNT
58523.5	339.4	17.776(264)	...	...	...	...	...	AAVSO
58535.4	351.3	17.661(230)	...	...	...	...	...	AAVSO
58549.4	365.3	17.177(108)	...	...	...	...	...	AAVSO
58556.4	372.3	14.930(009)	...	...	...	...	...	TNT
58563.4	379.3	14.254(011)	...	13.980(009)	...	...	...	TNT
58564.4	380.3	14.167(009)	...	13.882(007)	...	...	...	TNT
58567.4	383.3	14.269(007)	...	13.960(007)	...	...	...	TNT
58569.4	385.3	14.294(012)	14.108(009)	14.040(010)	13.944(008)	...	13.813(011)	TNT
58573.4	389.3	14.345(007)	14.085(009)	14.050(009)	13.985(009)	...	13.888(009)	TNT
58575.4	391.3	14.391(007)	14.219(008)	14.157(008)	14.173(006)	...	13.969(007)	TNT
58576.3	392.2	14.548(006)	...	14.220(008)	...	...	...	TNT
58577.4	393.3	14.516(010)	...	14.296(009)	...	...	...	TNT
58578.4	394.3	14.720(011)	...	14.340(008)	...	...	...	TNT
58581.3	397.2	14.889(012)	...	14.537(013)	...	...	...	TNT
58583.3	399.2	14.888(008)	...	14.641(011)	...	...	...	TNT
58587.3	403.2	15.124(009)	14.853(008)	14.801(007)	14.754(009)	...	14.718(009)	TNT
58590.3	406.2	...	15.051(131)	14.858(116)	...	...	...	TNT
58595.3	411.2	15.548(043)	15.456(056)	15.348(054)	15.261(046)	...	...	TNT
58604.3	420.2	16.659(023)	16.236(011)	16.337(016)	16.363(015)	...	15.989(012)	TNT
58605.3	421.2	16.592(020)	16.410(012)	16.260(015)	16.211(011)	...	16.041(014)	TNT
58606.3	422.2	16.864(031)	16.560(018)	16.604(022)	16.469(015)	...	16.350(021)	TNT
58607.3	423.2	16.992(119)	16.718(116)	16.639(088)	16.539(107)	...	16.640(183)	TNT
58609.3	425.2	17.496(058)	17.229(031)	17.115(039)	17.026(029)	...	16.830(034)	TNT
58610.3	426.2	17.239(032)	17.150(022)	16.889(023)	16.789(017)	...	16.657(026)	TNT
58611.2	427.1	17.778(089)	...	17.537(065)	...	...	...	TNT
58611.3	427.2	...	17.699(079)	...	17.208(041)	...	16.930(036)	TNT
58613.2	429.1	18.653(184)	18.232(104)	18.019(097)	17.502(037)	...	17.336(056)	TNT
58624.2	440.1	18.294(446)	17.748(145)	17.968(233)	17.271(098)	...	16.971(076)	TNT
58631.3	447.2	18.692(412)	18.375(168)	18.068(106)	17.700(063)	...	17.382(068)	TNT
58634.3	450.2	18.740(529)	...	18.045(133)	...	...	...	TNT
58638.3	454.2	...	...	18.001(086)	...	...	...	TNT
58644.2	460.1	18.573(160)	18.266(120)	18.035(176)	17.806(078)	...	...	TNT
58644.3	460.2	...	...	...	...	...	17.487(058)	TNT
58645.3	461.2	18.436(732)	...	...	...	...	...	TNT
58648.2	464.1	...	18.174(118)	17.801(095)	...	...	...	TNT
58663.4	479.3	18.623(030)	...	17.954(039)	...	...	...	AZT
58664.2	480.1	...	18.368(115)	18.250(182)	17.781(047)	...	17.320(048)	TNT
58665.2	481.1	18.607(187)	18.272(060)	18.190(066)	17.601(037)	...	17.179(035)	TNT
58669.8	485.7	18.620(027)	...	17.949(031)	...	...	...	AZT
58675.3	491.2	18.612(032)	...	17.961(028)	...	...	...	AZT
58684.7	500.6	18.940(028)	...	18.183(029)	...	...	...	AZT
58708.7	524.6	15.552(005)	...	...	...	14.959(003)	...	Yaoan
58710.7	526.6	14.836(004)	...	...	...	14.324(002)	...	Yaoan
58711.7	527.6	14.833(004)	...	...	...	14.299(002)	...	Yaoan
58720.8	536.7	14.395(012)	...	...	...	13.667(003)	...	Yaoan

<sup>a</sup> Days relative to the initial optical outburst (UT March 06.58 2018 = MJD 58184.08).Note: Uncertainties, in units of 0.001 mag, are 1 $\sigma$ .



**Table A3.** *Swift* Photometry of MAXI J1820+070

MJD	Phase <sup>a</sup>	<i>uvw2</i> (mag)	<i>uvm2</i> (mag)	<i>uvw1</i> (mag)	<i>UVOT u</i> (mag)	<i>UVOT v</i> (mag)
58191	7	12.37(07)	...	13.10(06)	12.52(07)	12.46(07)
58192	8	11.98(09)	12.18(07)	12.00(07)	12.12(07)	12.63(09)
58193	9	11.86(07)	13.55(11)	...	12.10(07)	...
58194	10	11.75(07)	11.90(09)	11.88(08)	12.11(07)	...
58195	11	11.50(07)	11.84(09)	...	11.79(07)	...
58197	13	11.43(07)	11.55(09)	...	11.76(07)	...
58198	14	11.42(07)	11.58(09)	...	11.66(07)	...
58199	15	11.30(09)	11.48(09)	11.35(07)	...	...
58201	17	11.34(09)	11.49(07)	11.28(07)	...	...
58202	18	11.17(09)	11.28(07)	11.19(07)	...	...
58204	20	11.24(09)	11.34(07)	11.09(07)	...	...
58206	22	11.03(09)	11.15(07)	11.08(08)	...	...
58208	24	11.32(09)	...	11.32(07)	...	...
58210	26	11.42(09)	11.52(07)	11.29(07)	...	...
58215	31	11.46(09)	11.58(07)	11.48(07)	...	...
58217	33	11.62(09)	...	...	...	...
58219	35	11.48(09)	...	...	...	...
58222	38	11.59(09)	...	...	...	...
58225	41	...	...	...	12.21(12)	...
58226	42	11.63(09)	12.39(10)	...	...	...
58227	43	...	...	11.94(10)	...	...
58229	45	...	...	12.15(10)	12.40(11)	...
58230	46	12.12(09)	...	...	...	...
58231	47	12.04(09)	...	...	...	...
58238	54	12.13(09)	...	...	...	...
58239	55	11.95(09)	...	...	...	...
58241	57	12.04(09)	...	...	11.95(07)	...
58243	59	...	12.19(07)	...	...	...
58244	60	11.97(09)	...	...	...	...
58248	64	...	...	...	12.19(11)	...
58259	75	...	...	...	12.56(11)	...
58259	75	...	...	...	12.40(10)	...
58268	84	13.33(09)	...	...	...	...
58270	86	12.83(09)	...	...	...	...
58272	88	12.92(09)	...	...	...	...
58276	92	12.87(09)	...	...	...	...
58294	110	12.69(09)	...	...	...	...
58306	122	...	...	...	12.46(10)	...
58307	123	12.38(09)	12.58(07)	12.49(07)	12.50(07)	13.54(06)
58308	124	12.50(09)	12.54(07)	12.39(07)	12.31(07)	13.46(06)
58309	125	...	...	...	12.67(11)	...
58310	126	...	...	...	12.45(11)	...
58311	127	12.17(09)	12.32(07)	12.28(07)	12.17(09)	13.24(06)
58312	128	...	...	...	12.26(11)	...
58324	140	...	12.58(07)	12.41(07)	12.38(08)	13.43(06)
58329	145	12.15(09)	12.32(07)	12.19(07)	12.15(08)	13.27(06)
58332	148	12.14(09)	...	12.21(07)	...	...
58334	150	...	12.43(07)	12.25(07)	12.23(08)	13.34(06)
58335	151	12.22(09)	12.42(07)	12.30(07)	12.25(08)	13.26(06)
58337	153	12.37(09)	12.48(07)	12.30(07)	12.32(08)	13.35(06)
58339	155	...	12.47(07)	12.33(07)	12.32(07)	13.38(06)
58363	179	12.58(09)	...	12.51(07)	12.48(07)	...
58369	185	12.77(09)	12.91(07)	12.80(07)	12.72(07)	13.76(06)
58379	195	12.85(09)	13.03(07)	12.94(07)	12.99(07)	...
58383	199	13.20(09)	13.28(07)	13.25(07)	14.23(06)	14.27(06)
58386	202	13.21(09)	13.36(07)	13.22(07)	13.23(07)	14.26(06)
58388	204	13.22(09)	13.38(07)	13.26(07)	13.28(07)	14.19(06)
58390	206	13.39(09)	13.56(07)	13.53(07)	13.50(07)	14.52(06)
58391	207	13.43(09)	13.71(07)	13.55(07)	13.69(07)	14.57(06)
58393	209	13.49(09)	13.66(07)	13.59(07)	13.73(07)	14.63(06)
58395	211	13.63(09)	13.77(07)	13.71(07)	13.84(07)	14.82(07)
58397	213	13.72(09)	13.92(07)	13.79(07)	13.83(07)	14.76(07)
58400	216	13.54(09)	13.74(08)	13.59(07)	13.62(08)	14.33(07)

<sup>a</sup> Days relative to the initial optical outburst (UT March 06.58 2018 = MJD 58184.08).Note: Uncertainties, in units of 0.01 mag, are  $1\sigma$ .

**Table A3** – *continued* A table continued from the previous one.

MJD	Phase <sup>a</sup>	<i>uvw2</i> (mag)	<i>uvm2</i> (mag)	<i>uvw1</i> (mag)	<i>UVOT u</i> (mag)	<i>UVOT v</i> (mag)
58402	218	13.54(09)	13.58(08)	13.40(07)	13.41(07)	14.11(07)
58404	220	13.46(09)	13.60(07)	13.43(07)	13.39(07)	14.07(06)
58407	223	13.66(09)	13.75(07)	13.65(07)	13.61(07)	14.29(06)
58408	224	13.62(09)	13.73(07)	13.54(07)	13.62(07)	14.24(06)
58410	226	13.68(09)	13.77(07)	13.62(07)	13.56(07)	14.35(06)
58412	228	13.74(09)	13.85(07)	13.69(07)	13.63(07)	14.42(06)
58417	233	13.94(09)	14.06(07)	13.91(07)	13.91(07)	14.70(06)
58420	236	14.09(09)	14.15(07)	14.00(07)	14.05(07)	14.73(06)
58422	238	14.13(09)	14.21(07)	14.11(07)	...	...
58425	241	14.28(09)	14.38(08)	14.26(07)	14.26(07)	15.01(07)
58428	244	14.35(09)	14.46(07)	14.36(07)	14.35(07)	15.09(06)
58431	247	14.59(09)	14.62(08)	14.48(07)	14.57(07)	15.23(07)
58433	249	14.63(10)	14.78(09)	14.49(08)	14.43(06)	15.31(09)
58434	250	14.83(09)	14.92(08)	14.77(07)	14.70(07)	15.58(07)
58437	253	14.87(09)	15.04(08)	14.91(07)	14.77(07)	15.53(07)
58439	255	15.14(09)	15.28(08)	14.94(07)	14.86(07)	15.87(07)
58440	256	15.21(09)	15.43(08)	15.25(08)	15.21(07)	15.98(07)
58546	362	18.99(15)	18.81(16)	18.26(13)	17.89(12)	18.15(15)
58552	368	17.21(10)	17.13(10)	16.57(09)	...	...
58559	375	13.76(09)	13.82(07)	13.68(07)	13.69(07)	14.31(06)
58566	382	13.44(09)	13.60(07)	13.33(07)	13.41(07)	14.01(06)
58576	392	...	...	...	13.68(07)	...
58591	407	...	14.58(07)	...	...	...
58602	418	15.54(11)	...	...	...	...
58607	423	...	...	16.35(07)	...	...
58612	428	...	...	17.65(10)	...	...
58614	430	18.54(13)	...	...	...	...
58615	431	...	...	18.01(20)	17.57(15)	...
58616	432	18.88(19)	18.28(19)	17.97(12)	17.67(09)	...
58620	436	...	...	18.21(11)	...	...
58622	438	...	18.75(13)	...	...	...
58626	442	18.78(13)	...	...	...	...

<sup>a</sup> Days relative to the initial optical outburst (UT March 06.58 2018 = MJD 58184.08).Note: Uncertainties, in units of 0.01 mag, are  $1\sigma$ .

**Table A4.** Log of Spectroscopic Observations of MAXI J1820+070

MJD	Phase <sup>a</sup>	Range (Å)	Disp. (Å/pix)	Telescope+Inst.
58195.93	11.85	3483-8745	2.85	LJT+YFOSC
58196.86	12.78	3971-8822	2.78	XLT+BFOSC
58196.93	12.85	3493-8750	2.85	LJT+YFOSC
58198.92	14.84	3483-8742	2.85	LJT+YFOSC
58201.81	17.73	3967-8823	2.78	XLT+BFOSC
58201.92	17.84	3491-8749	2.85	LJT+YFOSC
58207.83	23.75	3489-8743	2.85	LJT+YFOSC
58209.85	25.77	3489-8744	2.85	LJT+YFOSC
58211.82	27.74	3489-8743	2.85	LJT+YFOSC
58212.83	28.75	3486-8743	2.85	LJT+YFOSC
58223.86	39.78	3488-8745	2.85	LJT+YFOSC
58224.76	40.68	3971-8828	2.78	XLT+BFOSC
58224.76	40.68	3971-8828	2.78	XLT+BFOSC
58226.82	42.74	3980-8828	2.78	XLT+BFOSC
58226.83	42.75	3980-8827	2.78	XLT+BFOSC
58227.78	43.70	3972-8826	2.78	XLT+BFOSC
58227.80	43.72	3972-8826	2.78	XLT+BFOSC
58227.82	43.74	3972-8826	2.78	XLT+BFOSC
58236.74	52.66	3967-8823	2.78	XLT+BFOSC
58236.76	52.68	3969-8824	2.78	XLT+BFOSC
58245.81	61.73	3974-8827	2.78	XLT+BFOSC
58246.82	62.74	4004-8872	2.78	XLT+BFOSC
58282.75	98.67	3979-8830	2.78	XLT+BFOSC
58296.61	112.53	3971-8822	2.78	XLT+BFOSC
58296.63	112.55	3973-8824	2.78	XLT+BFOSC
58297.66	113.59	3969-8821	2.78	XLT+BFOSC
58297.68	113.60	3969-8821	2.78	XLT+BFOSC
58297.69	113.61	3970-8822	2.78	XLT+BFOSC
58297.71	113.63	3969-8821	2.78	XLT+BFOSC
58297.72	113.64	3970-8822	2.78	XLT+BFOSC
58297.74	113.66	3970-8822	2.78	XLT+BFOSC
58386.55	202.47	3850-8700	2.78	XLT+BFOSC
58390.46	206.38	3854-8701	2.78	XLT+BFOSC
58390.48	206.40	3854-8701	2.78	XLT+BFOSC
58390.50	206.42	3854-8701	2.78	XLT+BFOSC
58392.46	208.38	3852-8698	2.78	XLT+BFOSC
58392.48	208.40	3852-8698	2.78	XLT+BFOSC
58392.50	208.42	3852-8698	2.78	XLT+BFOSC
58395.46	211.38	3970-8697	2.78	XLT+BFOSC
58395.48	211.40	3970-8696	2.78	XLT+BFOSC
58396.49	212.41	3973-8699	2.78	XLT+BFOSC
58396.50	212.42	3973-8699	2.78	XLT+BFOSC
58399.44	215.36	3970-8696	2.78	XLT+BFOSC
58399.46	215.38	3970-8696	2.78	XLT+BFOSC
58400.45	216.37	3973-8699	2.78	XLT+BFOSC
58400.47	216.39	3973-8699	2.78	XLT+BFOSC
58401.45	217.37	3976-8701	2.78	XLT+BFOSC
58401.47	217.39	3976-8701	2.78	XLT+BFOSC
58404.48	220.40	5139-8776	4.8	XLT+OMR
58409.44	225.36	3762-8689	4.8	XLT+OMR
58421.49	237.41	3976-8698	2.78	XLT+BFOSC
58431.41	247.33	3856-8699	2.78	XLT+BFOSC
58435.44	251.36	3855-8701	2.78	XLT+BFOSC
58441.48	257.40	3486-8747	2.85	LJT+YFOSC
58444.42	260.34	3857-8704	2.78	XLT+BFOSC
58446.42	262.34	3853-8698	2.78	XLT+BFOSC
58447.42	263.34	3855-8699	2.78	XLT+BFOSC
58555.82	371.74	4358-8710	2.78	XLT+BFOSC
58559.81	375.73	3860-8825	2.78	XLT+BFOSC
58559.86	375.78	3862-8825	2.78	XLT+BFOSC
58564.81	380.73	3863-8826	2.78	XLT+BFOSC
58564.84	380.76	3866-8829	2.78	XLT+BFOSC
58566.85	382.77	3861-8826	2.78	XLT+BFOSC
58568.83	384.75	3863-8827	2.78	XLT+BFOSC
58568.85	384.77	3864-8828	2.78	XLT+BFOSC
58568.86	384.78	3864-8828	2.78	XLT+BFOSC

<sup>a</sup> Days relative to the initial optical outburst (UT March 06.58 2018 = MJD 58184.08).